Improving Calibration of EMG-Informed Neuromusculoskeletal Models Through Differentiable Physics and Muscle Synergies

Author

Hambly, MJ, Worsey, MTO, Lloyd, DG, Pizzolato, C

Published

2025

Journal Title

IEEE Transactions on Biomedical Engineering

Version

Accepted Manuscript (AM)

DOI

10.1109/TBME.2025.3569682

Improving Calibration of EMG-Informed Neuromusculoskeletal Models Through Differentiable Physics and Muscle Synergies

Matthew J. Hambly*, Matthew T. O. Worsey, David G. Lloyd, and Claudio Pizzolato

Abstract*—*Objective: **Electromyogram (EMG)-informed neuromusculoskeletal (NMS) models can predict physiologically plausible muscle forces and joint moments. However, calibrating model parameters (e.g., optimal fiber length, tendon slack length) to the individual is time-consuming, with the optimization often requiring hours to converge and typically not accounting for unrecorded muscle excitations. This study addresses these limitations by incorporating differentiable physics and muscle synergies into the calibration of NMS models.** ***Methods:*** **We implemented an NMS model with auto-differentiable Hill-type muscles, enabling the use of adaptive gradient descent optimizers. Two types of calibration were evaluated: a standard EMG-driven approach and a synergy-hybrid approach that also synthesized unrecorded excitations. These methods were evaluated using upper and lower limb data, each from a single participant.** ***Results:*** **The calibration time was reduced by up to 26 times while maintaining comparable accuracy in moment predictions. Compared to the EMG-driven calibration, the synergy-hybrid calibration improved the estimates of model parameters for reduced number of EMG channels.** ***Conclusion:*** **Auto-differentiable Hill-type muscle models greatly reduce NMS model calibration time and enables the synthesis of unrecorded muscle excitations through muscle synergies, facilitating the calibration of all muscle parameters.** ***Significance:*** **This new rapid calibration could support deployment of NMS models in time-sensitive applications, including real-time biomechanical analyses and personalized neurorehabilitation.**

***Index Terms*—Neuromusculoskeletal modeling, calibration, differential physics, muscle synergies.**

I. Introduction

NEUROMUSCULOSKELETAL (NMS) modeling offers a physics-based mathematical framework to simulate the complex and dynamic interactions between the neural, muscular, and skeletal systems [1, 2]. When informed by electromyograms (EMG), NMS models also account for individual-specific motor control, and predict muscle forces in response to EMG variations even when the observed kinematics and kinetics remain unchanged [3]. This physics-based framework has broad applications for injury prevention [4-6], rehabilitation [7-9], orthopedic surgical planning [10, 11], and as a human-centered control paradigm for exoskeletons [12] and electrical stimulation of muscles [13]. However, prior to their use, EMG-informed NMS models require calibration of neuromuscular parameters (e.g., optimal fiber length, tendon slack length, etc.) to best reflect the physiology of the individual and improve prediction accuracy [1, 14, 15]. Stochastic optimization algorithms such as simulated annealing [16] or particle swarm [17] have been traditionally used to calibrate NMS models [14], but they are extremely slow to converge - up to multiple hours [18].

Another limitation of NMS model calibration is that it requires EMG data from all modeled muscles. This is impractical, as numerous sensors are needed, and some muscles are difficult to access for recording. EMG-assisted NMS approaches partially address this limitation by synthesizing missing EMG signals and minimally adjusting recorded EMGs to optimize the differences between predicted and recorded joint moments [14, 19]. While these techniques mitigate some challenges associated with limited EMG recordings during the NMS model execution, they may inadequately reflect how muscle parameters were adjusted during calibration. A three-stage calibration process [6, 13, 20] has been used to address this issue, consisting of an initial calibration, followed by an EMG-assisted execution to synthesize unrecorded excitations, and finally calibrating all muscles using both recorded and synthesized EMGs. However, this process is time-consuming and complex, introducing multiple points where errors can occur.

A promising solution to these challenges is muscle synergy analysis, which identifies the underlying neural patterns in recorded EMG signals from individuals. This creates synergies with a reduced number of time-varying neural commands, known as primitives [21, 22], and a set of scalar muscle weightings. Primitives and weights are extracted from recorded EMG data via factorization methods, such as non-negative matrix factorization [23, 24], and have been used to extrapolate a full set of muscle excitations from a limited number of EMG recordings [25] and to drive NMS models [24, 26]. Although

This study was supported by the Motor Accident Insurance Commission, Queensland, Australia (BioSpine project) and by a Griffith University Postgraduate Research Scholarship.

Matthew J. Hambly, Matthew T.O. Worsey, David G. Lloyd, and Claudio Pizzolato are with The Australian Centre for Precision Health and Technology, Queensland, Australia, and the School of Health Sciences and Social Work, Griffith University, Queensland, Australia. * (correspondence e-mail: matthew.hambly@griffithuni.edu.au).

recent emerging methods have begun to explore similar concepts [27, 28], it remains largely unexplored whether NMS modeling could be used to optimize primitives and weightings to reconstruct recorded excitations and synthesize unrecorded excitations, while improving joint moment tracking. Embedding such an approach into NMS model calibration would enable generating physiologically plausible muscle excitations while simultaneously optimizing model parameters.

Reducing calibration time and the number of required EMG recordings could be achieved by embedding neural network techniques into physics-based models, an approach known as differentiable physics [29]. Differentiable physics-based models are compatible with backpropagation through automatic-differentiation, which allows calculating the gradients of the loss function with respect to the model parameters [30, 31]. The gradients can then be used to optimize the parameters through efficient gradient descent approaches (e.g., adaptive moment estimation with weight decay [32]), commonly used to train large neural networks [33].

This study aimed to implement an auto-differentiable EMG-informed NMS model to enhance calibration. We first evaluated the efficacy of using backpropagation and gradient descent optimization to reduce calibration time. We then extended the calibration process to simultaneously synthesize missing EMG recordings using muscle synergies while calibrating all model parameters.

II. Auto-differentiable EMG-informed NMS model

The auto-differentiable NMS model was integrated into the NMS modeling framework in the CEINMS toolbox [14], coded in C++. This implementation (Fig. 1) allows the prediction of muscle-tendon unit (MTU) forces and joint moments using recorded data, including muscle excitations, MTU lengths, and moment arms as inputs.

Backpropagation through the model was performed using LibTorch [34], with the torch::Tensor class enabling automatic differentiation. To enhance computational efficiency, the NMS model was reformulated to exploit tensor matrix operations, calculating the Hadamard product (∘) of the matrices. The model inputs, intermediate states, and outputs are represented as $\mathrm{N_m} \times \mathrm{N_t}$ matrices, where $\mathrm{N_m}$ denotes the number of muscles and $\mathrm{N_t}$ is the number of trials. Similarly, the model parameters are expressed as $\mathrm{N_m}$ arrays. This approach allows the model to evaluate all muscles and trials in parallel at each timestep.

Muscle activations are computed from the normalized linear envelope of EMG recordings, i.e., muscle excitations. First, a critically-damped linear second-order differential system models the neural activation ($\boldsymbol{u}$, a $\mathrm{N_m} \times \mathrm{N_t}$ matrix) from the excitation, as shown in [1]:

$$\begin{gathered} \boldsymbol{u}_i = \boldsymbol{\alpha} \circ \boldsymbol{e}_{i-d^{em}} - \boldsymbol{\beta_1} \circ \boldsymbol{u}_{i-1} - \boldsymbol{\beta_2} \circ \boldsymbol{u}_{i-2} \\ \boldsymbol{\beta_1} = \boldsymbol{C_1} + \boldsymbol{C_2} \\ \boldsymbol{\beta_2} = \boldsymbol{C_1} \circ \boldsymbol{C_2} \\ \boldsymbol{\alpha} = 1 + \boldsymbol{\beta_1} + \boldsymbol{\beta_2} \end{gathered} \tag{1}$$

where i is the timestep, $\boldsymbol{e}$ ($\mathrm{N_m} \times \mathrm{N_t}$ matrix) is the muscle excitations, d^{em} is the electromechanical delay, and $\boldsymbol{C_1}$ and $\boldsymbol{C_2}$ ($\mathrm{N_m}$ arrays) are recursive coefficients. Subsequently, the muscle activation ($\boldsymbol{a}$, a $\mathrm{N_m} \times \mathrm{N_t}$ matrix) is obtained from the neural activation using an exponential relationship [1]:

$$\boldsymbol{a}_i = \frac{e^{\boldsymbol{A} \circ \boldsymbol{u}_i} - 1}{e^{\boldsymbol{A}} - 1} \tag{2}$$

where $\boldsymbol{A}$ (N_m array) is a non-linear shape factor constrained in the interval (-3, 0). An appropriate electromechanical delay is selected and fixed (d^{em} = 35 ms) based on our prior modeling to ensure minimal impact on the prediction of experimental data

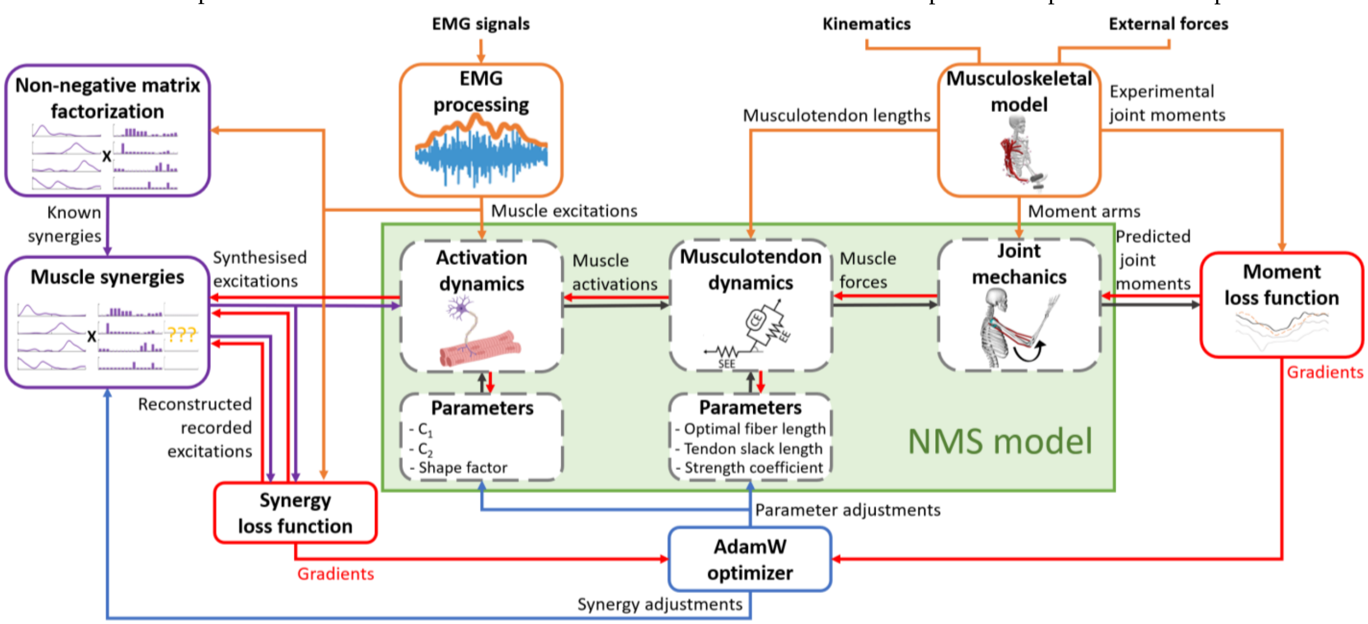

Fig. 1. Overview of the differentiable physics neuromusculoskeletal (NMS) model calibration. Recorded electromyograms (EMG), kinematics, and forces are processed as model inputs. Muscle excitations drive activations, which along with musculotendon lengths, predict muscle forces. Joint moments are calculated from forces and moment arms, then compared to inverse dynamics moments. Gradients of model parameters and synergies (red lines) are computed via backpropagation for calibration using gradient descent. In EMG-driven calibration, only recorded excitations are used, while in synergy-hybrid calibration, muscle synergies are extracted and optimized to synthesize unrecorded excitations.

[35], while the parameters $\boldsymbol{C_1}$, $\boldsymbol{C_2}$ and $\boldsymbol{A}$ are typically found through calibration [1, 14, 36].

The force generated by the muscle is calculated using a Hill-type muscle model from the activation and MTU length [1, 2]:

$$\boldsymbol{F_i^m} = \boldsymbol{F^{max}} \circ \cos(\boldsymbol{\phi}_i) \circ \left[F^a(\boldsymbol{\tilde{l}_i^m}) \circ F^v(\boldsymbol{\tilde{v}_i^m}) \circ \boldsymbol{a}_i + F^p(\boldsymbol{\tilde{l}_i^m}) + \boldsymbol{d^m} \circ \boldsymbol{\tilde{v}_i^m}\right] \quad (3)$$

where $\boldsymbol{F^m}$ ($\mathrm{N_m} \times \mathrm{N_t}$ matrix) is the force generated by the MTU, $\boldsymbol{F^{max}}$ ($\mathrm{N_m}$ array) is the maximum isometric force, $\boldsymbol{\tilde{l}^m}$ and $\boldsymbol{\tilde{v}^m}$ ($\mathrm{N_m} \times \mathrm{N_t}$ matrices) are the normalized muscle length and velocity respectively, $\boldsymbol{d^m}$ ($\mathrm{N_m}$ array) is the damping, $\boldsymbol{\phi}$ ($\mathrm{N_m} \times \mathrm{N_t}$ matrix) is the pennation angle, and F^a, F^p and F^v are the active and passive length, and velocity force curves respectively [37]. Fiber length is normalized to the optimal fiber length, while fiber velocity is normalized to the product of the optimal fiber length and maximum contraction velocity. The muscle fiber length was calculated using a Rosenbrock elastic tendon model [38], which is detailed in Appendix A along with the muscle model validation.

Finally, the joint moment is calculated using traditional matrix multiplication, where the force from each muscle acting on a degree of freedom (DOF) is multiplied by its respective moment arm, and the results are summed across all muscles.

III. Enhanced NMS model calibration

A. *Experimental data description and processing*

The data used for the evaluation of the NMS modeling in this paper includes a single participant from a publicly available upper limb dataset [39] (age 33 years, body mass 68.5 kg, height 1.8 m). The lower limb data were collected from a single participant (28 years, 51 kg, 1.61 m). For the latter, the protocol was approved by the Griffith University Human Research Ethics Committee (GU ethics no 2022/762).

The upper limb dataset [39] was collected using six marker clusters placed on the thorax, scapula, humerus, forearm, and hand recorded at 100 Hz using an Optotrak system (Northern Digital, Inc., Ontario, Canada). EMG data were recorded with surface electrodes (Ambu N-00-S ECG), sampled at 1000 Hz using a 16-channel Porti system (TMS International, Enschede, Netherlands), sites prepared according to SENIAM guidelines [40]. EMG were acquired from anterior, medial and posterior deltoid, clavicular and sternal pectoralis major, infraspinatus, latissimus dorsi, biceps brachii short head, triceps brachii medial and long heads, and brachioradialis. Maximum voluntary contraction (MVC) of the muscles were recorded [41]. Recorded data included multiple trials of range of movement tasks during shoulder abduction, shoulder rotation end elbow flexion.

For the lower limb data, 31 individual markers and 25 clustered markers were used to capture motion data of the full body. These data were recorded at 200 Hz using a Vicon 10-camera (MX T40-S) motion capture system (Vicon Motion Systems, Oxford, UK), while ground reaction forces (GRF) were synchronously measured at 1000 Hz using an instrumented treadmill (AMTI, Massachusetts, USA). A single leg was prepared following SENIAM guidelines for synchronous recording of 14 EMG signals at 2000 Hz (Aktos, Myon, Switzerland). EMG were acquired from the biceps femoris long head, gastrocnemius lateralis and medialis, gluteus maximus and medius, gracilis, rectus femoris, sartorius, semimembranosus, soleus, tensor fasciae latae, tibialis anterior, and vastus lateralis and medialis. Data were collected during MVCs and while the participant walked at a self-selected pace, and +5% and +15% of base pace, across multiple gait cycles.

Marker data, GRFs, and EMGs were processed using OpenSim (Version 4.4) [42] and MOtoNMS [43]. Generic models of the upper [44, 45] and lower [46, 47] limb were linearly scaled using anthropometric measurements and markers during a static pose. The scaled models were then used to perform inverse kinematics to calculate joint angles, inverse dynamics to determine joint moments, and muscle analysis for MTU lengths and moment arms estimation. The EMG signals were band-pass filtered between 30 and 300 Hz using a 3rd order Butterworth filter to remove noise, rectified and lowpass filtered at 5 Hz using a 4th order Butterworth filter to obtain the linear envelopes [48, 49], then normalized to the MVC trials. Each trial, containing multiple movement cycles, was segmented into individual cycles using peak finding methods for kinematic data (upper limb) and GRFs (lower limb).

Uncalibrated NMS models were constructed using the linearly scaled OpenSim model parameters for the MTUs. Only the MTUs with a corresponding recorded EMG mapping, as summarized in the supplementary material (Table SI), were included in the NMS model. The upper limb NMS model contained three DOFs: shoulder elevation, shoulder rotation, and elbow flexion. The lower limb NMS model also contained three DOFs: hip, knee, and ankle flexion.

B. *EMG-driven calibration*

EMG-driven calibration was performed by two optimization methods: CEINMS EMG-driven calibration [14] and differentiable physics EMG-driven calibration. The standard CEINMS EMG-driven calibration uses simulated annealing, whereas the differentiable physics calibration used an AdamW optimizer [32], a decoupled weight decay variant of the commonly used Adam gradient descent optimizer [50]. Differentiable physics calibration employed a decaying learning rate and an early stopping criterion, halting when the loss function ceased improving for a predefined number of iterations. Details on the learning rate and early stopping setting for the AdamW optimizer are provided in the supplementary material (Table SII). Both calibration approaches minimized the error between inverse dynamics and NMS model predicted joint moments by adjusting NMS model parameters.

Both EMG-driven calibration methods adjusted the same NMS model parameters. These were the typical recursive coefficients (C_1 and C_2) and shape factor (A) from the activation dynamics, and the optimal fiber length, tendon slack length and a strength coefficient to scale the maximum isometric force (F^{max}) from the MTU dynamics. MTUs were grouped for common strength coefficient scaling, while other parameters were calibrated per MTU. The two EMG-driven calibration methods minimized the following loss function [14] (F^{cal}):

$$F^{cal} = \sum_{t}^{N_t} \frac{1}{N_i} \sum_{i}^{N_i} \left[\begin{array}{c} \frac{1}{N_d} \sum_{d}^{N_d} \left(\bar{M}_{t,i,d} - M_{t,i,d} \right)^2 + \\ \sum_{m}^{N_m} \left(P^{l}_{t,i,m}\left(\tilde{l}^m\right) + P^{\varepsilon}_{t,i,m}\left(\varepsilon^t\right) \right) \end{array} \right] \quad (4)$$

$$P = \begin{cases} w(x^{min} - x)^2, & x < x^{min} \\ w(x - x^{max})^2, & x > x^{max} \\ 0, & otherwise \end{cases}$$

where N_t, N_i, N_d and N_m are the number of trials, timesteps, DOFs and MTUs respectively, $\bar{M}$ is the inverse dynamics moment, M is the NMS model predicted moment, P^l and P^{ε} are the penalty functions for the normalized fiber length and tendon strain respectively, penalizing values (x) outside of the operative range (x^{min}, x^{max}), applying a weighting (w). The differentiable physics calibration optimization settings are summarized in the supplementary material (Table SII).

C. Synergy-hybrid calibration

To incorporate all MTUs in the calibration, unrecorded excitations were synthesized using muscle synergies. Initial trial-specific primitives and muscle weightings were derived from non-negative matrix factorization [23, 24], with weightings for unrecorded MTUs randomized. Calibration minimized the error between reconstructed and recorded excitations while synthesizing unrecorded excitations to help track inverse dynamics joint moments. The recorded EMG excitations were still used to drive their respective MTUs, while synergies synthesized excitations to drive the remaining MTUs. Synthesized excitations, primitives, and muscle weightings were constrained between zero and one using the penalty function P (Eq. 4), while an additional term was included to minimize the contribution of the synthesized excitations similar to EMG-hybrid NMS model execution techniques [14, 19]. As such, the following loss function was minimized during synergy-hybrid calibration:

$$F^{cal} = \sum_{t}^{N_t} \frac{1}{N_i} \sum_{i}^{N_i} \left[\begin{array}{c} \frac{1}{N_d} \sum_{d}^{N_d} \left(\bar{M}_{t,i,d} - M_{t,i,d} \right)^2 \\ + P_{t,i} + F^{exc}_{t,i} \end{array} \right] \quad (5)$$

$$F^{exc}_{t,i} = \frac{1}{N_r} \sum_{r}^{N_r} w^e \left(\bar{e}_{t,i,r} - e_{t,i,r} \right)^2 + \frac{1}{N_s} \sum_{s}^{N_s} w^s e^2_{t,i,s}$$

where $P_{t,i}$ represents all of the penalty functions (i.e., normalized fiber length, tendon strain, excitations, primitives and muscle weightings), N_r and N_s are the number of recorded and synthesized excitations respectively, w^e and w^s are the weights for the recorded excitation tracking and synthesized excitation minimization respectively. Optimization settings are summarized in the supplementary material (Table SII).

D. Overview and comparisons of the NMS model calibrations

In summary, there were three calibration approaches examined: CEINMS EMG-driven, differentiable physics EMG-driven, and differentiable physics synergy-hybrid calibrations. All methods were used to calibrate the upper and lower limb NMS models. For the upper limb model a single cycle each of shoulder abduction, shoulder rotation and elbow flexion were used, while for the lower limb a single stance phase during walking gait at the three different speeds were used, with the same trials used for each calibration methods.

The three calibration approaches incorporated multiple ways to encourage physiologically plausible MTU models. For instance, muscles nominally generate active force within a normalized fiber length range of 0.5 to 1.5 [2]. The calibration penalty functions constrained normalized fiber lengths to operate on the ascending limb and plateau of the force-length relationship, consistent with prior physiological evidence [51-53]. Physiological fiber lengths and tendon slack lengths were further reinforced by ensuring MTUs, particularly two-joint MTUs, operated in a physiologically and mechanically consistent manner across multiple joints and degrees of freedom during calibration and execution [36]. Finally, the CEINMS EMG-driven calibration did not include the tendon strain penalty, it used an equilibrium elastic tendon model, opposed to both of the differentiable physics calibration methods that employed an auto-differentiable model (see Appendix A). The tendon strain penalty constrained the tendon strain values within the range of a default tendon force-strain curve (i.e., 0 to 0.5) [37], preventing non-physiological negative tendon and muscle fiber lengths during calibration, while facilitating physiological zero muscle activations [37, 38, 54] with the differentiable physics method.

The three calibration approaches were assessed based on model accuracy, similarity in model parameters and calibration time. Model accuracy was evaluated using root mean squared error (RMSE) and coefficient of determination (R^2) between the inverse dynamics and NMS model predicted joint moments. To assess the effect of replacing recorded excitations with synthesized values, we compared the accuracy and final model parameters. Synergy-reconstructed excitations were directly compared to experimentally recorded excitations.

After CEINMS and differentiable physics EMG-driven calibration, the models were executed using an EMG-driven method to evaluate model accuracy. This is an open-loop method where muscle forces and joint moments are predicted based on the recorded excitations [1] in CEINMS, using trials that were not part of the calibration. For the upper limb model, nine trials of shoulder abduction, four trials of shoulder rotation and six trials of elbow flexion were used, while for the lower limb model, 16 stance phase trials at the baseline self-selected speed were used. RMSE and R^2 were averaged across all movement cycles within each range of movement task.

Pre-empting that the CEINMS and differentiable physics EMG-driven calibration yielded similar modeling accuracy, the synergy-hybrid approach was directly compared to the differentiable physics EMG-driven calibration using a reduced set of excitations. Recorded excitations, thus MTUs based on the EMG mapping (Table SI), were singularly removed from multiple EMG-driven calibrations. The rank order of the lowest

This article has been accepted for publication in IEEE Transactions on Biomedical Engineering. This is the author's version which has not been fully edited and content may change prior to final publication. Citation information: DOI 10.1109/TBME.2025.3569682

to highest RMSE, averaged across DOFs and calibration trials was used to determine the removal order for subsequent evaluation. The NMS models were then calibrated using the differential physics EMG-driven and synergy-hybrid calibrations, sequentially removing the ordered excitations. Seven and four synergies were used for the upper and lower limb models, respectively. This was determined from initial pilot testing detailed in the supplementary material (Fig. S1), where the variance accounted for between the experimental and synergy reconstructed excitations was greater than 85% [22]. RMSE and R^2 were calculated for each number of recorded excitations, averaging across trials and DOFs. Additionally, the calibrated model MTU parameters (optimal fiber length, tendon slack length, and strength coefficient) were compared to those of a model calibrated using the differentiable physics EMG-driven approach with all recorded excitations. Each parameter was normalized to the allowable range, and the absolute difference between the optimal and reduced excitation models were averaged across all parameters and MTUs.

The time taken during each calibration was measured to assess the computational speed. All calibrations were run on a Windows PC with 12th Gen Intel® Core™ i9-12900K processor (3.20 GHz, 16 core) and 64 GB of RAM.

For statistical analyses, a Shapiro-Wilk test [55] was used to determine whether each data group was normally distributed. For normally distributed data an independent sample t-test was used, while a Mann-Whitney U test was used for data not normally distributed. For all statistical analysis, the significance level was set to $p < 0.05$.

IV. Results

The differentiable physics calibration methods were between 13 and 26 times faster than CEINMS EMG-driven calibration (Fig. 2). For the upper limb model, there was no significant differences in joint moment RMSE or R^2 between the EMG-driven CEINMS and differentiable physics calibration (Fig. 3). For the lower limb model, the differentiable physics calibration resulted in significantly lower RMSE and higher R^2 for hip flexion, and higher RMSE and lower R^2 for knee and ankle flexion compared to CEINMS (Fig. 3).

In the synergy-hybrid calibration, the extracted synergies (Fig. 4) led to significantly lower RMSE than the EMG-driven calibration when only two MTUs received recorded excitations for the upper limb model (Fig. 5). Additionally, higher R^2 values were observed when between two and eight MTUs had recorded excitations for the upper limb model (Fig. 5). The EMG-driven calibration produced significantly lower difference in model parameters than the hybrid approach for the upper limb model with only one recorded excitation (Fig. 5). For the lower limb model, the synergy calibration approach produced significantly lower RMSE with three and two recorded excitations, and significantly higher R^2 with eight, four, three and two recorded excitations, while the EMG-driven approach provided significantly lower RMSE with only one recorded excitation (Fig. 5).

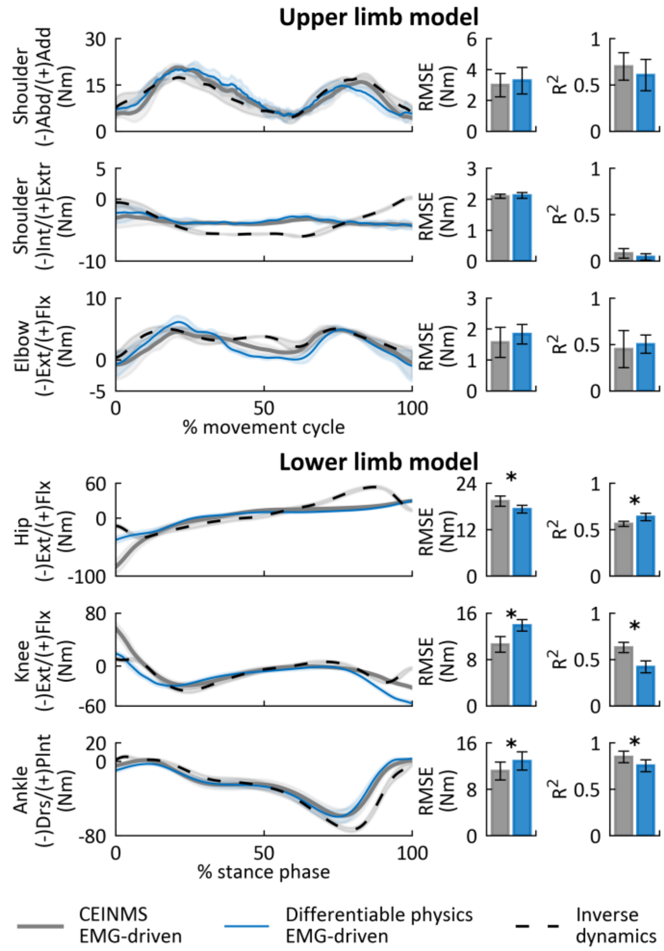

Fig. 3. Joint moment tracking accuracy of the EMG-driven calibrated upper and lower limb models. Abd=abduction, Add=adduction, Int=internal rotation, Extr=external rotation, Ext=extension, Flx=flexion, Drs=dorsiflexion, Plnt=plantar flexion.

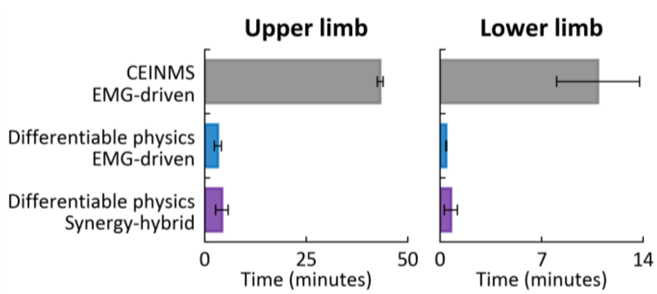

Fig. 2. Time to calibrate upper and lower limb NMS models using CEINMS EMG-driven, differentiable physics EMG-driven and synergy-hybrid methods. The differentiable physics calibration times were averaged across all EMG-driven and synergy-hybrid testing, while the CEINMS time was averaged across 10 repetitions of the EMG-driven test.

V. Discussion

In this study we implemented an auto-differentiable EMG-informed NMS model, demonstrating its potential to improve the calibration process. We first validated the approach against an EMG-driven calibration using the traditional CEINMS and differentiable physics approaches. We then extended it to a synergy-hybrid approach to calibrate MTUs without recorded excitations, showcasing the flexibility and robustness of the auto-differentiable model.

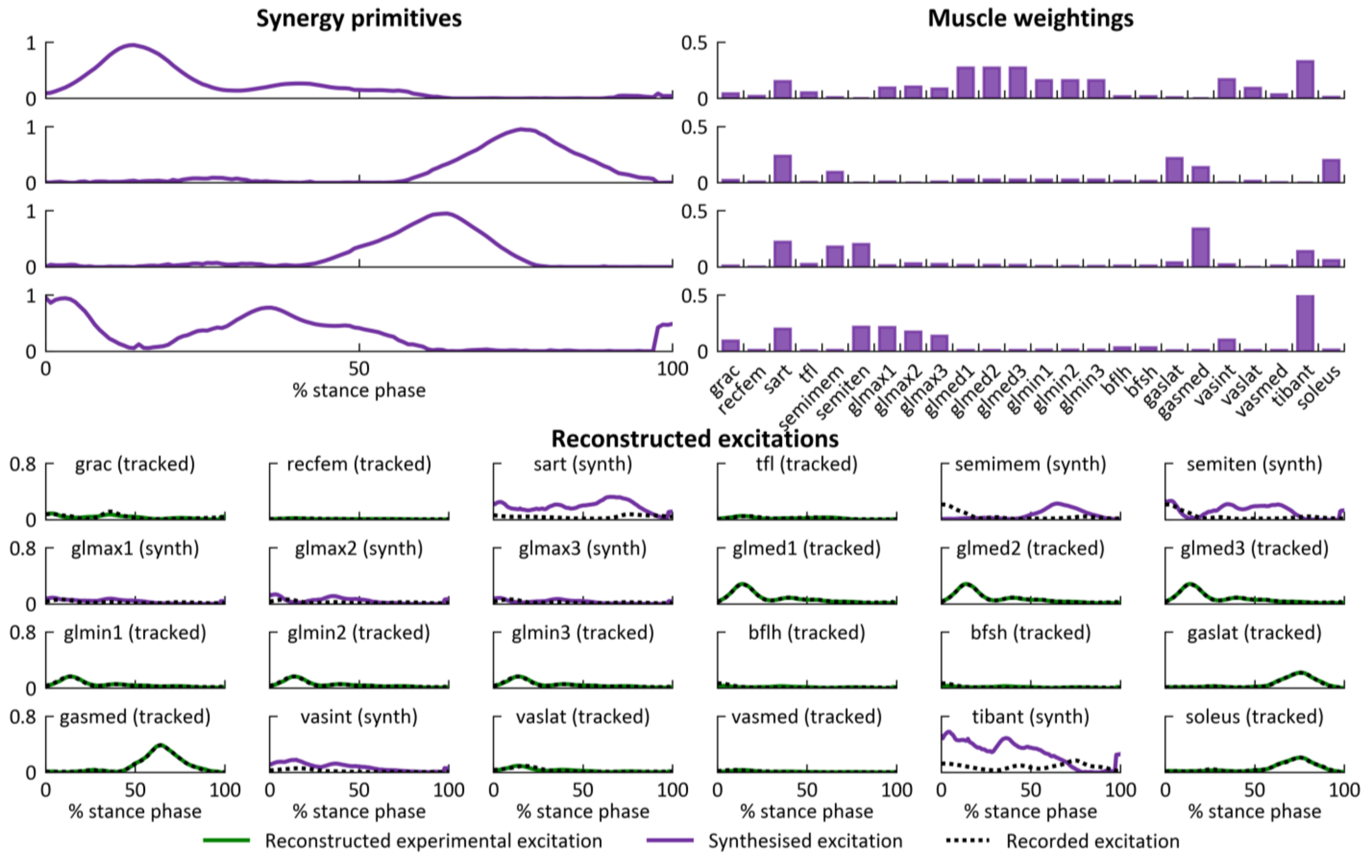

Fig. 4. Example synergy extraction and reconstruction of muscle excitations from the lower limb calibration testing with five recorded EMG recording removed.

Across all DOFs and trials, the proposed differentiable physics EMG-driven calibration demonstrated accuracy comparable to models calibrated using simulated annealing in CEINMS (Fig. 3). Both calibration methods demonstrated low accuracy for estimating shoulder rotation and failed to capture the hip flexion moment peak towards the end of the stance phase (Fig. 3), likely due to limited EMG recordings from critical muscles (e.g., supraspinatus, subscapularis, teres minor, teres major and coracobrachialis for the upper limb, and the iliacus and psoas for the lower limb). The addition of other loss functions (e.g., minimizing the peak of summed forces [56] or maximizing moment tracking R^2) may improve the performance of the differentiable physics calibration in the future. The proposed method exhibited an approximately 13-fold reduction in calibration time for the upper limb model and 26-fold reduction for the lower limb model (Fig. 2). Furthermore, the use of efficient matrix operations in the NMS model provided improved computation performance as the number of calibration trials increased (Fig. S2). Traditionally, the calibration process presented a major barrier to using NMS modeling for real-time applications, potentially requiring hours to wait for the calibration to converge before being able to execute the NMS model. The substantial decrease in calibration time demonstrated here could enable the real-time application of NMS models, providing immediate performance feedback across a range of fields—from elite sports, enhancing athlete performance, to neurorehabilitation for spinal cord injury patients, optimizing recovery outcomes.

The synergy-hybrid calibration, which synthesizes unrecorded excitations (Fig. 4), showed superior joint moment tracking ability compared to the EMG-driven calibration. This improvement in joint moment tracking achieved by the synergy-hybrid approach helps mitigate the reduced accuracy observed in the differentiable physics EMG-driven approach when compared to the CEINMS approach (Fig. 3). Importantly, synergy-hybrid calibrated models closely matched those calibrated with all excitations recorded (Fig. 5). However, there were cases where EMG-driven calibration resulted in parameters that more closely matched the optimal, all excitations model, particularly in the upper limb data (Fig. 5). This could be due to the low EMG amplitude required for the tasks, leading to minimal differences when replaced with no EMG. Moreover, omitting certain EMG recordings could significantly affect the extraction of muscle synergies, including the ability to accurately reconstruct recorded signals and synthesize unrecorded signals. In this work, we evaluated the synergy-hybrid calibration by sequentially removing recorded excitations in order of their effect on calibration accuracy. However, future investigation is required to identify the minimal number and optimal selection of EMGs to ensure robust calibration across different joints and tasks [24, 36]. Additionally, the synergy-hybrid calibration could be used to more effectively map excitation signals to individual MTUs, rather than assuming the same excitations as nearby muscles[1, 14, 36]. Overall, the proposed synergy-hybrid calibration provides a method that better represents all muscles compared to the standard EMG-driven calibration, also providing a simple and efficient alternative to the three-stage calibration used previously [6, 13, 20].

The implementation of differentiable physics enables many

This article has been accepted for publication in IEEE Transactions on Biomedical Engineering. This is the author's version which has not been fully edited and content may change prior to final publication. Citation information: DOI 10.1109/TBME.2025.3569682

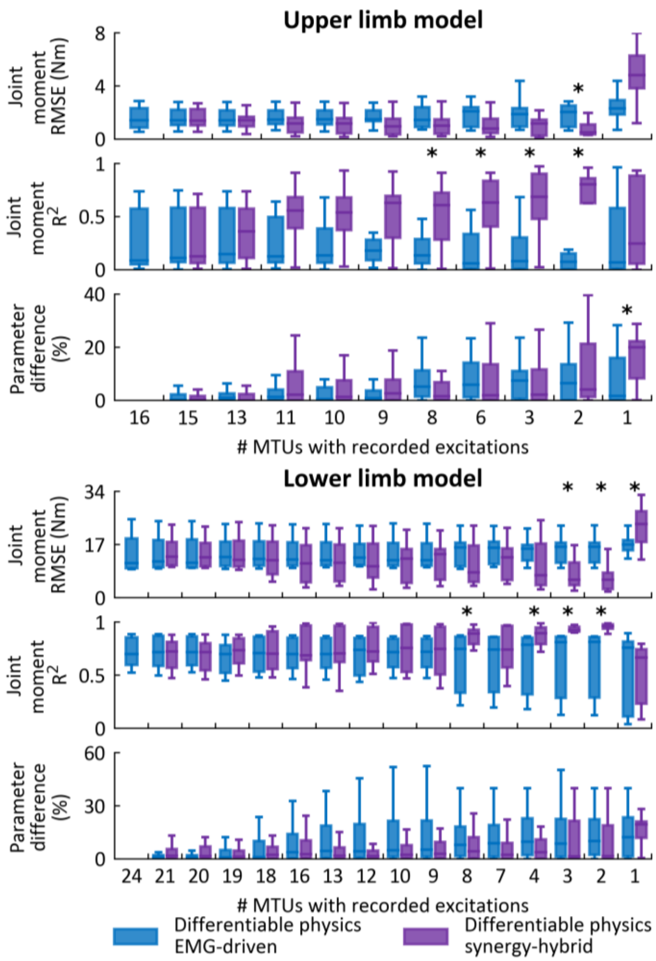

Fig. 5. Joint moment tracking accuracy and similarity of model parameters using EMG-driven and synergy hybrid calibration with differentiable physics as recorded muscle excitations are removed from the calibration.

opportunities to explore and expand how we use NMS modeling. While differentiable models have been developed in the past, they used symbolic differentiation [38], limiting model extensibility and flexibility in handling different topologies. In contrast, our auto-differentiable model enables modifications to the loss function as needed, allowing for seamless implementation of different loss functions or underlying modeling dynamics (e.g., activation dynamics [54, 57]). The new formulation with increased efficiency could facilitate simultaneous calibration and execution. As shown in the supplementary material (Fig. S3), the loss decreases rapidly in early iterations, suggesting that a reduced number of iterations could reduce calibration time with a modest trade-off in accuracy, although further investigation is required. Additionally, instead of a single prolonged calibration, multiple shorter calibrations could be performed across data windows, refining the model incrementally and improving robustness over time. Such an approach would enable real-time, subject specific NMS modeling without prior calibration and allow for dynamic adjustments of model parameters to reflect changes, such as fatigue [18]. The scalability of differentiable physics through parallelization could also support the calibration and execution of larger-scale models, including motor unit-level models [58], while also potentially benefiting from GPU utilization for improved performance with more complex models. Neural networks can be integrated into the auto-differentiable NMS model to compensate for areas where traditional physics-based models fall short, such as low-fidelity or sparse input data, and incomplete or simplified physics [59]. For instance, while the physics model may rely on assumptions for joint kinematics or MTU dynamics, neural networks can capture complex, nonlinear relationships from data, compensating for inaccuracies and improving predictions. Additionally, the flexibility of auto-differentiation allows surrogate models (e.g., approximating MTU kinematics [60], joint kinematics [61, 62] and/or joint tissue loading [63]) to be seamlessly integrated and optimized within the same framework, combining the strengths of both approaches.

Some limitations should be acknowledged. The calibration was only evaluated using data from two participants, one each for the upper and lower limb models. However, the use of two different datasets and the subject-specific nature of the modeling suggest that the findings could be transferable to other individuals. Previous studies have successfully applied similar methods to populations with cerebral palsy [24, 64], osteoarthritis [65-67], and anterior cruciate ligament reconstruction [68], demonstrating the applicability of NMS models across diverse demographics, including children and individuals with clinical conditions. Another limitation is the incomplete EMG dataset, as recordings were not available for all muscles contributing to upper and lower limb movements. Surface EMG has inherent limitations in recording signals from deeper muscles due to factors like muscle depth, size, and the potential for crosstalk [19, 69, 70]. Future studies might require intramuscular electrodes to capture a more comprehensive set of EMG signals from which initial synergies could be extracted. In the current study we did not assess the effect of the calibration methods on different execution methods (e.g., EMG-assisted), including only analyzing the calibration accuracy of the synergy-hybrid calibration method. Further evaluation of these methods during execution is warranted. Also, although the preferred method [22], we only evaluated non-negative matrix factorization for synergy extraction, which was able to consistently extract similar synergies as outlined in the supplementary material (Fig. S4 and Fig. S5). Other techniques, such as representing synergies as Gaussian curves [26], may offer improved efficiency by reducing the number of variables requiring optimization, offering a promising direction to be explored further. Moreover, while an 85% variance accounted for threshold has been shown to be appropriate for determining the required number of synergies using non-negative matrix factorization [22], further criteria could be considered to refine this selection [71], particularly for different tasks and limb segments. Nevertheless, the synergy method does constrain calibration to experimentally observed muscle excitation patterns, whereas EMG-assisted methods resort to more traditional static optimization (e.g., minimization of the squared excitation), which may lead to predicted excitations that deviate more from physiologically plausible muscle excitations. Finally, while MTU parameters are often initialized using pre-optimization or muscle volume-based scaling [72, 73], these steps were not included in the current calibration process due to their impact on calibration time. Incorporating them in future work could enhance physiological plausibility, but more efficient methods would be required.

VI. Conclusion

We successfully implemented and validated an auto-differentiable EMG-informed NMS model, using differential physics and back-propagation. The new formulation allowed for the efficient calibration of model parameters, achieving prediction accuracies comparable to the standard EMG-driven calibration approach while significantly reducing calibration time. Additionally, the ability to synthesize unrecorded excitations during calibration via muscle synergies enabled accurate parameter estimation for all muscles, even with incomplete EMG data. These advancements in EMG-informed NMS model calibration unlock new possibilities for real-time applications, such as in neurorehabilitation, and pave the way for integration with hybrid physics-informed neural networks.

Appendix A

To calculate the muscle fiber length in the auto-differentiable NMS model, we implemented a first order Rosenbrock elastic tendon method [38], backpropagation compatible. The detailed derivation is reported in [38] and summarized here in terms of the muscle fiber length. In the Rosenbrock formulation, the function f describes the relationship between current state (x), its derivative and a control (u) in implicit form:

$$f\left(x+\Delta x, \frac{\Delta x}{h}, u+\Delta u\right)=0 \qquad (A1)$$

which can be expanded using a first order Taylor series expansion, substituting in the derivative of the state ($\dot{x}$):

$$f(x,\dot{x},u)+\frac{\partial f}{\partial x}\Delta x+\frac{\partial f}{\partial \dot{x}}\left(\frac{\Delta x}{h}-\dot{x}\right)+\frac{\partial f}{\partial u}\Delta u=0 \qquad (A2)$$

and rearranged in terms of the change in state:

$$\Delta x=\left(\frac{\partial f}{\partial x}+\frac{1}{h}\frac{\partial f}{\partial \dot{x}}\right)^{-1}\left(\frac{\partial f}{\partial \dot{x}}\dot{x}-f(x,\dot{x},u)-\frac{\partial f}{\partial u}\Delta u\right) \qquad (A3)$$

$$x_{i+1}=x_i+\left(\frac{\partial f}{\partial x}+\frac{1}{h}\frac{\partial f}{\partial \dot{x}}\right)^{-1}\cdot$$
$$\left(\frac{\partial f}{\partial \dot{x}}\dot{x}_i-f(x_i,\dot{x}_i,u_i)-\frac{\partial f}{\partial u}(u_{i+1}-u_i)\right) \qquad (A4).$$

The derived equation is then applied to calculate the new muscle fiber length as

$$l_{i+1}^m=l_i^m+\left(\frac{\partial f}{\partial l^m}+\frac{1}{h}\frac{\partial f}{\partial v^m}\right)^{-1}\cdot$$
$$\left(\frac{\partial f}{\partial v^m}v^m-f(l_i^m,v_i^m,a_i)-\frac{\partial f}{\partial a}(a_{i+1}-a_i)\right) \qquad (A5)$$
$$f(l^m,v^m,a)=F^t(l^m)-F^m(l^m,v^m,a) \qquad (A6)$$

where F^T is the tendon force from the force-strain curve [37] scaled by the maximum isometric force. Here the partial differentials are solved through automatic differentiation using the LibTorch library [34]. If the tendon length is shorter than the tendon slack length, the tendon strain is zero, potentially leading to erroneous fiber lengths. Previous studies have employed constraints such as non-zero activation or active force, or a minimum fiber length [37, 38, 54]; however, these assumptions may not be physiologically accurate. Here, we extend the tendon force-strain curve beyond zero strain and penalize negative strain values during calibration to avoid non-physiological solutions.

We validated the Rosenbrock elastic tendon model following the method previously used to validate the equilibrium elastic tendon model [37]. Ex-vivo muscle forces were measured from the soleus muscle of a rat and cat during maximal and submaximal activations, respectively, with varying levels of maximal displacement [74, 75]. For maximal activation trials, model parameters were optimized using an AdamW optimizer on the largest displacement trial minimizing the mean absolute error between predicted and recorded forces [37], while penalizing tendon strain outside of the expected range. Reported measurements were used as the parameters for the

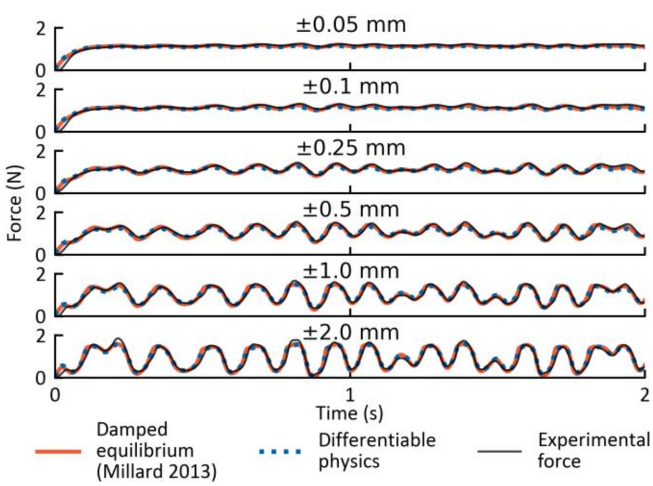

Fig. 6. Predicted force with damped equilibrium and auto-differentiable elastic tendon models, compared to experimental force in maximal activation.

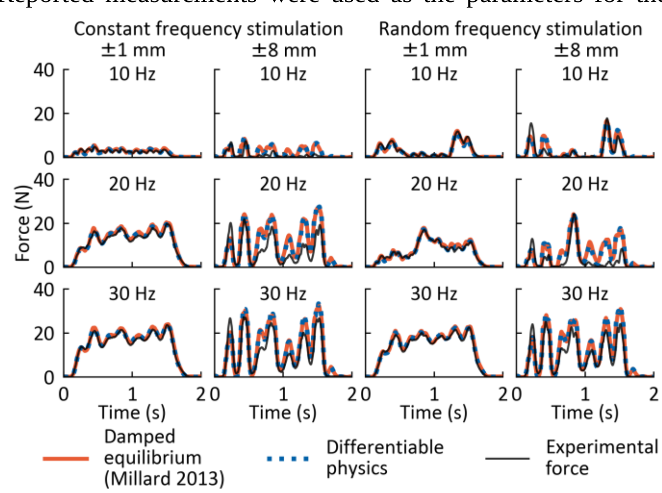

Fig. 7. Predicted force with damped equilibrium and auto-differentiable elastic tendon models, compared to experimental force in submaximal activation.

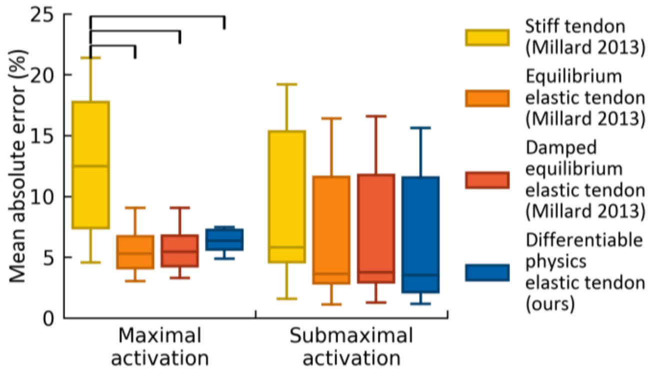

Fig. 8. Force prediction using the stiff, equilibrium elastic, damped equilibrium elastic and auto-differentiable elastic tendon models. Horizontal bars signify a statistically significant difference between the models.

submaximal trials [76]. For the maximal activation validation we used the same simplified first order activation dynamics as used in [37], allowing us to validate the new elastic tendon formulation within the MTU dynamics. For the submaximal activation validation the same input activation signal from [37] was used to drive the model.

For each trial, the mean absolute error was calculated between the predicted and experimental forces, normalized to the experimentally measured maximum isometric force. The errors were compared to results of the stiff tendon, equilibrium, and damped equilibrium models reported in [37], averaged across trials within the maximal and submaximal datasets. Data were normally distributed for the maximal activation trials and non-normally distributed for the submaximal trials; ANOVA and Kruskal-Wallis ANOVA tests were used, respectively.

Across all trials, the auto-differentiable model predicted muscle forces similar to the equilibrium model and experimental force (Fig. 6 and Fig. 7). In maximal activation trials, the stiff tendon model produced significantly greater mean absolute errors than all other models. while no statistically significant differences were observed in submaximal activation trials (Fig. 8).

Acknowledgment

The authors would like to thank Bradley Cornish for data collection and discussions to refine our study design.

References

[1] D. G. Lloyd, and T. F. Besier, "An EMG-driven musculoskeletal model to estimate muscle forces and knee joint moments in vivo," *Journal of biomechanics,* vol. 36, no. 6, pp. 765-776, 2003.
[2] F. E. Zajac, "Muscle and tendon: properties, models, scaling, and application to biomechanics and motor control," *Critical reviews in biomedical engineering,* vol. 17, no. 4, pp. 359-411, 1989.
[3] A. Kian *et al.*, "Static optimization underestimates antagonist muscle activity at the glenohumeral joint: A musculoskeletal modeling study," *Journal of Biomechanics,* vol. 97, pp. 109348, 2019.
[4] N. Assila *et al.*, "Glenohumeral joint and muscles functions during a lifting task," *Journal of biomechanics,* vol. 126, pp. 110641, 2021.
[5] A. Moya-Esteban *et al.*, "Muscle-level analysis of trunk mechanics via musculoskeletal modeling and high-density electromyograms." pp. 1109-1114.
[6] P. Silvestros *et al.*, "Electromyography-assisted neuromusculoskeletal models can estimate physiological muscle activations and joint moments across the neck before impacts," *Journal of Biomechanical Engineering,* vol. 144, no. 3, pp. 031011, 2022.
[7] C. Pizzolato *et al.*, "Biofeedback for gait retraining based on real-time estimation of tibiofemoral joint contact forces," *IEEE Transactions on Neural Systems and Rehabilitation Engineering,* vol. 25, no. 9, pp. 1612-1621, 2017.
[8] T. J. Collings *et al.*, "Gluteal Muscle Forces during Hip-Focused Injury Prevention and Rehabilitation Exercises," *Medicine and Science in Sports and Exercise,* vol. 55, no. 4, pp. 650-660, 2023.
[9] D. Devaprakash *et al.*, "Free Achilles tendon strain during selected rehabilitation, locomotor, jumping, and landing tasks," *Journal of Applied Physiology,* vol. 132, no. 4, pp. 956-965, 2022.
[10] A. K. Dastgerdi *et al.*, "Surgical parameters influence paediatric knee kinematics and cartilage stresses in anterior cruciate ligament reconstruction: Navigating subject-specific variability using neuromusculoskeletal-finite element modelling analysis," *Knee Surgery, Sports Traumatology, Arthroscopy*, 2024.
[11] E. Eghan-Acquah *et al.*, "Enhancing Biomechanical Outcomes in Proximal Femoral Osteotomy through Optimised Blade Plate Sizing: A Neuromusculoskeletal-Informed Finite Element Analysis," *Computer Methods and Programs in Biomedicine*, pp. 108480, 2024.
[12] G. Durandau *et al.*, "Voluntary control of wearable robotic exoskeletons by patients with paresis via neuromechanical modeling," *Journal of neuroengineering and rehabilitation,* vol. 16, no. 1, pp. 1-18, 2019.
[13] M. J. Hambly *et al.*, "EMG-Informed Neuromusculoskeletal Modelling Estimates Muscle Forces and Joint Moments During Electrical Stimulation." pp. 1-6.
[14] C. Pizzolato *et al.*, "CEINMS: A toolbox to investigate the influence of different neural control solutions on the prediction of muscle excitation and joint moments during dynamic motor tasks," *Journal of biomechanics,* vol. 48, no. 14, pp. 3929-3936, 2015.
[15] A. Kian *et al.*, "The effectiveness of EMG-driven neuromusculoskeletal model calibration is task dependent," *Journal of Biomechanics,* vol. 129, pp. 110698, 2021.
[16] A. Corana *et al.*, "Minimizing multimodal functions of continuous variables with the "simulated annealing" algorithm—Corrigenda for this article is available here," *ACM Transactions on Mathematical Software (TOMS),* vol. 13, no. 3, pp. 262-280, 1987.
[17] J. F. Schutte *et al.*, "Evaluation of a particle swarm algorithm for biomechanical optimization," 2005.
[18] M. I. Mohamed Refai *et al.*, "Electromyography-driven musculoskeletal models with time-varying fatigue dynamics improve lumbosacral joint moments during lifting," *Journal of Biomechanics,* vol. 164, pp. 111987, 2024/02/01/, 2024.
[19] M. Sartori *et al.*, "Hybrid neuromusculoskeletal modeling to best track joint moments using a balance between muscle excitations derived from electromyograms and optimization," *Journal of biomechanics,* vol. 47, no. 15, pp. 3613-3621, 2014.
[20] M. Romanato *et al.*, "Influence of different calibration methods on surface electromyography-informed musculoskeletal models with few input signals," *Clinical Biomechanics,* vol. 109, pp. 106074, 2023.
[21] N. Lambert-Shirzad, and H. M. Van der Loos, "On identifying kinematic and muscle synergies: a comparison of matrix factorization methods using experimental data from the healthy population," *Journal of neurophysiology,* vol. 117, no. 1, pp. 290-302, 2017.
[22] M. F. Rabbi *et al.*, "Non-negative matrix factorisation is the most appropriate method for extraction of muscle synergies in walking and running," *Scientific reports,* vol. 10, no. 1, pp. 1-11, 2020.
[23] D. Lee, and H. S. Seung, "Algorithms for non-negative matrix factorization," *Advances in neural information processing systems,* vol. 13, 2000.
[24] M. F. Rabbi *et al.*, "Muscle synergy-informed neuromusculoskeletal modelling to estimate knee contact forces in children with cerebral palsy," *Biomechanics and Modeling in Mechanobiology,* vol. 23, no. 3, pp. 1077-1090, 2024.
[25] M. F. Rabbi *et al.*, "A muscle synergy-based method to estimate muscle activation patterns of children with cerebral palsy using data collected from typically developing children," *Scientific reports,* vol. 12, no. 1, pp. 3599, 2022.
[26] M. Sartori *et al.*, "A musculoskeletal model of human locomotion driven by a low dimensional set of impulsive excitation primitives," *Frontiers in computational neuroscience,* vol. 7, pp. 79, 2013.
[27] D. Ao *et al.*, "EMG-driven musculoskeletal model calibration with estimation of unmeasured muscle excitations via synergy extrapolation," *Frontiers in Bioengineering and Biotechnology*, pp. 1533, 2022.

[28] M. Romanato *et al.*, "Muscle synergies to reduce the number of electromyography channels in neuromusculoskeletal modelling: a pilot study," *bioRxiv*, pp. 2024.09. 24.614668, 2024.

[29] B. Ramsundar *et al.*, "Differentiable physics: A position piece," *arXiv preprint arXiv:2109.07573*, 2021.

[30] C. M. Bishop, "Neural networks and their applications," *Review of scientific instruments,* vol. 65, no. 6, pp. 1803-1832, 1994.

[31] J. G. Greener *et al.*, "A guide to machine learning for biologists," *Nature Reviews Molecular Cell Biology,* vol. 23, no. 1, pp. 40-55, 2022.

[32] I. Loshchilov, and F. Hutter, "Decoupled weight decay regularization," *arXiv preprint arXiv:1711.05101*, 2017.

[33] S. Ruder, "An overview of gradient descent optimization algorithms," *arXiv preprint arXiv:1609.04747*, 2016.

[34] A. Paszke *et al.*, "Pytorch: An imperative style, high-performance deep learning library," *Advances in neural information processing systems,* vol. 32, 2019.

[35] T. N. Savage *et al.*, "Neuromusculoskeletal model calibration accounts for differences in electromechanical delay and maximum isometric muscle force," *Journal of Biomechanics,* vol. 149, pp. 111503, 2023.

[36] M. Sartori *et al.*, "EMG-driven forward-dynamic estimation of muscle force and joint moment about multiple degrees of freedom in the human lower extremity," *PloS one,* vol. 7, no. 12, pp. e52618, 2012.

[37] M. Millard *et al.*, "Flexing computational muscle: modeling and simulation of musculotendon dynamics," *Journal of biomechanical engineering,* vol. 135, no. 2, pp. 021005, 2013.

[38] A. J. Van Den Bogert *et al.*, "Implicit methods for efficient musculoskeletal simulation and optimal control," *Procedia Iutam,* vol. 2, pp. 297-316, 2011.

[39] B. Bolsterlee *et al.*, "Modelling clavicular and scapular kinematics: from measurement to simulation," *Medical & biological engineering & computing,* vol. 52, pp. 283-291, 2014.

[40] H. J. Hermens *et al.*, "European recommendations for surface electromyography," *Roessingh research and development,* vol. 8, no. 2, pp. 13-54, 1999.

[41] C. E. Boettcher *et al.*, "Standard maximum isometric voluntary contraction tests for normalizing shoulder muscle EMG," *Journal of orthopaedic research,* vol. 26, no. 12, pp. 1591-1597, 2008.

[42] A. Seth *et al.*, "OpenSim: Simulating musculoskeletal dynamics and neuromuscular control to study human and animal movement," *PLoS computational biology,* vol. 14, no. 7, pp. e1006223, 2018.

[43] A. Mantoan *et al.*, "MOtoNMS: A MATLAB toolbox to process motion data for neuromusculoskeletal modeling and simulation," *Source code for biology and medicine,* vol. 10, pp. 1-14, 2015.

[44] K. R. Holzbaur *et al.*, "A model of the upper extremity for simulating musculoskeletal surgery and analyzing neuromuscular control," *Annals of biomedical engineering,* vol. 33, no. 6, pp. 829-840, 2005.

[45] D. C. McFarland *et al.*, "Spatial dependency of glenohumeral joint stability during dynamic unimanual and bimanual pushing and pulling," *Journal of biomechanical engineering,* vol. 141, no. 5, 2019.

[46] A. Rajagopal *et al.*, "Full-body musculoskeletal model for muscle-driven simulation of human gait," *IEEE transactions on biomedical engineering,* vol. 63, no. 10, pp. 2068-2079, 2016.

[47] S. D. Uhlrich *et al.*, "Muscle coordination retraining inspired by musculoskeletal simulations reduces knee contact force," *Scientific reports,* vol. 12, no. 1, pp. 9842, 2022.

[48] E. Langzam *et al.*, "Muscle enhancement using closed-loop electrical stimulation: Volitional versus induced torque," *Journal of Electromyography and Kinesiology,* vol. 17, no. 3, pp. 275-284, 2007.

[49] N. Assila *et al.*, "EMG-Assisted Algorithm to Account for Shoulder Muscles Co-Contraction in Overhead Manual Handling," *Applied Sciences,* vol. 10, no. 10, pp. 3522, 2020.

[50] D. P. Kingma, and J. Ba, "Adam: A method for stochastic optimization," *arXiv preprint arXiv:1412.6980*, 2014.

[51] M. H. Andrews *et al.*, "Multiscale hamstring muscle adaptations following 9 weeks of eccentric training," *Journal of sport and health science*, pp. 100996, 2024.

[52] K. Veerkamp *et al.*, "Comments on Harkness-Armstrong et al.(2021)'In vivo operating lengths of the gastrocnemius muscle during gait in children who idiopathically toe-walk'," *Experimental physiology,* vol. 107, no. 12, 2022.

[53] F. A. Panizzolo *et al.*, "Soleus fascicle length changes are conserved between young and old adults at their preferred walking speed," *Gait & posture,* vol. 38, no. 4, pp. 764-769, 2013.

[54] D. G. Thelen, "Adjustment of muscle mechanics model parameters to simulate dynamic contractions in older adults," *J. Biomech. Eng.,* vol. 125, no. 1, pp. 70-77, 2003.

[55] P. Mishra *et al.*, "Descriptive statistics and normality tests for statistical data," *Annals of cardiac anaesthesia,* vol. 22, no. 1, pp. 67, 2019.

[56] E. Meinders *et al.*, "Electromyography measurements of the deep hip muscles do not improve estimates of hip contact force," *Journal of Biomechanics,* vol. 141, pp. 111220, 2022.

[57] K. Manal, and T. S. Buchanan, "An electromyogram-driven musculoskeletal model of the knee to predict in vivo joint contact forces during normal and novel gait patterns," *Journal of biomechanical engineering,* vol. 135, no. 2, pp. 021014, 2013.

[58] A. H. Caillet *et al.*, "Motoneuron-driven computational muscle modelling with motor unit resolution and subject-specific musculoskeletal anatomy," *PLOS Computational Biology,* vol. 19, no. 12, pp. e1011606, 2023.

[59] M. Raissi *et al.*, "Physics-informed neural networks: A deep learning framework for solving forward and inverse problems involving nonlinear partial differential equations," *Journal of Computational physics,* vol. 378, pp. 686-707, 2019.

[60] B. M. Cornish *et al.*, "Real-time calibration-free musculotendon kinematics for neuromusculoskeletal models," *IEEE Transactions on Neural Systems and Rehabilitation Engineering*, 2024.

[61] B. Shi *et al.*, "Automatic generation of knee kinematic models from medical imaging," *Computer Methods and Programs in Biomedicine,* vol. 256, pp. 108370, 2024.

[62] M. Barzan *et al.*, "Development and validation of subject-specific pediatric multibody knee kinematic models with ligamentous constraints," *Journal of biomechanics,* vol. 93, pp. 194-203, 2019.

[63] A. Esrafilian *et al.*, "An automated and robust tool for musculoskeletal and finite element modeling of the knee joint," *IEEE Transactions on Biomedical Engineering*, 2024.

[64] G. Davico *et al.*, "Multi-level personalization of neuromusculoskeletal models to estimate physiologically plausible knee joint contact forces in children," *Biomechanics and modeling in mechanobiology,* vol. 21, no. 6, pp. 1873-1886, 2022.

[65] H. X. Hoang *et al.*, "A calibrated EMG-informed neuromusculoskeletal model can appropriately account for muscle co-contraction in the estimation of hip joint contact forces in people with hip osteoarthritis," *Journal of biomechanics,* vol. 83, pp. 134-142, 2019.

[66] L. Diamond *et al.*, "Individuals with mild-to-moderate hip osteoarthritis walk with lower hip joint contact forces despite higher levels of muscle co-contraction compared to healthy individuals," *Osteoarthritis and Cartilage,* vol. 28, no. 7, pp. 924-931, 2020.

[67] M. Hall *et al.*, "Effect of a valgus brace on medial tibiofemoral joint contact force in knee osteoarthritis with varus malalignment: A within-participant cross-over randomised study with an uncontrolled observational longitudinal follow-up," *Plos one*, vol. 17, no. 6, pp. e0257171, 2022.

[68] J. M. Konrath *et al.*, "Hamstring harvest results in significantly reduced knee muscular protection during side-step cutting two years after anterior cruciate ligament reconstruction," *Plos one,* vol. 18, no. 10, pp. e0292867, 2023.

[69] L. Mesin, "Crosstalk in surface electromyogram: literature review and some insights," *Physical and Engineering Sciences in Medicine,* vol. 43, pp. 481-492, 2020.

[70] J. Perry *et al.*, "Surface versus intramuscular electrodes for electromyography of superficial and deep muscles," *Physical therapy,* vol. 61, no. 1, pp. 7-15, 1981.

[71] K. Zhao *et al.*, "Muscle synergies for evaluating upper limb in clinical applications: A systematic review," *Heliyon,* vol. 9, no. 5, 2023.

[72] L. Modenese *et al.*, "Estimation of musculotendon parameters for scaled and subject specific musculoskeletal models using an optimization technique," *Journal of biomechanics,* vol. 49, no. 2, pp. 141-148, 2016.

[73] G. G. Handsfield *et al.*, "Relationships of 35 lower limb muscles to height and body mass quantified using MRI," *Journal of biomechanics,* vol. 47, no. 3, pp. 631-638, 2014.

[74] E. J. Perreault *et al.*, "Hill muscle model errors during movement are greatest within the physiologically relevant range of motor unit firing rates," *Journal of biomechanics,* vol. 36, no. 2, pp. 211-218, 2003.

[75] A. M. Krylow, and T. G. Sandercock, "Dynamic force responses of muscle involving eccentric contraction," *Journal of biomechanics,* vol. 30, no. 1, pp. 27-33, 1997.

[76] S. H. Scott *et al.*, "Mechanics of feline soleus: I. Effect of fascicle length and velocity on force output," *Journal of Muscle Research & Cell Motility,* vol. 17, pp. 207-219, 1996.